Structural characteristics of electrohydrodynamic jets induced by a blade-plane actuator subjected to highly non-uniform electric fields: Parametric investigation through the particle image velocimetry techniques

Zelu Yan, Christophe Louste, Philippe Traoré, Jian Wu, Jian'An Fang

Received: 9 June 2022 | Revised: 14 August 2022 | Accepted: 26 September 2022

DOI: 10.1049/hve2.12293

High Voltage

ORIGINAL RESEARCH

Structural characteristics of electrohydrodynamic jets induced by a blade-plane actuator subjected to highly non-uniform electric fields: Parametric investigation through the particle image velocimetry techniques

Zelu Yan[1] | Christophe Louste[2] | Philippe Traoré[2] | Jian Wu[3] | Jian'an Fang[4]

[1]Logistics Engineering College, Shanghai Maritime University, Shanghai, China

[2]Institut PPRIME, Université de Poitiers, Poitiers, France

[3]Key Laboratory of Aerospace Thermophysics, School of Energy Science and Engineering, Harbin Institute of Technology, Harbin, China

[4]College of Information Science and Technology, Donghua University, Shanghai, China

Correspondence

Zelu Yan, Logistics Engineering College, Shanghai Maritime University, 1550 Haigang Avenue, Shanghai 201306, China.
Email: zlyan@shmtu.edu.cn

Associate Editor: Mona Ghassemi

Funding information

National Natural Science Foundation of China, Grant/Award Number: 51907118

Abstract

This study set out to systematically investigate the structural characteristics of plane electrohydrodynamic jets through the particle image velocimetry (PIV) techniques. Due to the wide range of applied voltages and electrode gaps under various experimental conditions, an assessment of the image quality and a statistical analysis of the velocity fields are first performed to ensure the validity of the PIV measurements, which were originally applied purely to fluid mechanics. The results indicate that the time interval between two consecutive images should be pre-adjusted to reduce the number of uncorrelated vector fields. Moreover, the minimum number of instantaneous fields should be achieved for an accurate calculation of the time-averaged fields. An equivalent electric field criterion adapted to the asymmetric electrode configuration is defined to find similarities in flow structures under different voltage and electrode gap conditions. As the applied electric field increases, three injection regimes are identified and the current increases almost linearly, indicating a large conduction current component. The decrease in charge density due to recombination proves to be relevant in all cases of this study. Analogous to the parametric analysis approach for classical jets and thermal plumes, the evolution of the coefficients of axial velocity, half-width and turbulence intensity are investigated.

1 | INTRODUCTION

Electrohydrodynamic (EHD) flows are complex phenomena in which the electric and fluid fields are strongly coupled. The EHD effect describes the motion of the fluid due to the electric forces exerted on the electric charges in a dielectric liquid [1]. These charges are generated by injection, conduction and induction under intense electric fields. This so-called electroconvective flow shows an innovative and promising way in the direct conversion of electric energy into kinetic energy of dielectric liquids [2]. EHD-based applications, such as EHD pumping techniques demonstrate unique advantages over conventional mechanical pumping technologies, for example, low power consumption due to small currents in the microamp or milliamp range, potential meso-microscale design owing to small electrode size and flexible arrangement inside the pump, lightweight, no mechanical failure, low acoustic noise because of the absence of rotating machinery [3]. These pumps are capable of producing pressure heads of up to 2500 Pa and flow rates of up to 4000 mm^3/s, potentially contributing to enhanced heat and mass transfer and droplet transport of living biological cells [4, 5]. In the harsh space environment lacking atmospheric protection, the thermal control system is an important part to ensure the normal operation of the space station or satellite, in which the thermal control loop pump, as its core component, is equivalent to the 'heart' of the space station [6]. However, under the critical pressure in microgravity, the circulating centrifugal pump can

suffer from complex cavitation phenomena, which greatly affects the lifetime, safety and maintenance cost of the space station or satellite. In addition, it is more difficult to deal with liquid propellants, thermal control, wastewater management and recycling in microgravity conditions due to the complexity of controlling capillary forces [7]. To overcome these challenges, NASA has introduced the STP-H5 EHD single phase thermal pumping since 2016 [8], providing a future development solution for heat and mass transfer systems in space.

To better understand these EHD flows, significant progress has been made in theories related to the nature and origin of space charge [9, 10], in experiments related to flow and current measurements [11, 12], and in simulations associated with modelling [13], electroconvective instability [14] and verification of experiments [15–17]. The configuration of the actuator of the pump, the propriety of the dielectric liquid, and the applied signal can all play a significant role in determining injection strength, dissociation intensity, and flow structure. The actuator itself is composed of various types of electrodes, such as plane-plane, blade-plane line-plane, ball-plane and needle-plane. The research on the blade-plane geometry represent a growing field due to its two-dimensional structure that facilitates the in-depth study of the coupling features between charges and flow fields.

The EHD jet theory in the blade-plane geometry was developed with reference to the line-plane configuration [18]. Charged plume models for both laminar and turbulent regimes analogous to classical plumes were built theoretically to obtain asymptotic laws, that is, variations in characteristic velocity, mean charge density and plume width [10, 19]. These studies, as one of the first attempts to thoroughly describe the EHD flow structures, are of great importance for the future development of EHD models. Nevertheless, these models are valid for the whole flow field except near the active electrode, where the non-uniform electric field strength is extremely high and the charge formation mechanism has been debated ever since the establishment of the EHD interdisciplinary. More experimental studies are therefore needed.

One of the first non-intrusive optical measurements of this configuration is associated with the work in ref. [20], which investigated the relationship between velocity and electric power input. However, with the help of the Laser Doppler Anemometry, the velocity variation can be obtained at a single point instead of a vector map, which hinders a clear understanding of the entire flow field [21]. For more than a decade, the particle image velocimetry (PIV) techniques have been employed to capture the whole field properties of EHD plumes in the steady or transient regime [12]. The most problematic issue with this method arises from the tracer particles that are added to the fluid. These particles may be electrically charged and not follow the velocity of the flow field correctly. The movement of a charged particle is determined by various forces acting on it [22]. Theoretical calculations by the Basset-Boussinesq-Oseen equation have shown that the migration velocity of charged particles can be neglected in almost all regions with flow velocities. Experimental studies have shown that the electrical behaviour of the tracer particles is very weak when the concentration is below 0.15 g/L [23]. Therefore, with proper selection of tracer particles, the measurement error caused by the electric field on the liquid velocity can be safely neglected [23, 24].

Numerical investigations corresponding to experiments serve to study implicit features that may be difficult to identify in experiments, such as charge density distribution [25], charge injection strength [26] and ion evolution in the vicinity of the injector [17]. However, not all simulation results can be verified, as experimental studies pertaining to the EHD jet structures in the blade-plane geometry have not been systematic performed. Compared to fluid mechanics, the development of theoretical and numerical models usually lacks empirical support stemming from experimental parametrical studies, which is the overall aim of this paper.

The idea of choosing thermal plumes and classical jets as benchmarks for comparison is based on the following facts. First, the Coulomb force that sets the EHD jet in motion can be compared to the buoyant force, which is the main driver of the thermal plume [10, 18]. However, the main limitation of this analogy is that the buoyancy, although weak, still exists at great distances from the source, whereas the electric force, always large close to the source, decreases rapidly with distance [1]. Second, beyond a certain distance, the EHD jet moves downstream only by inertia and viscous effects, which looks more similar to a free jet.

2 | METHODOLOGY

2.1 | Experimental setup and measurement strategy

The experimental apparatus is shown in Figure 1. A cubical container (2) measuring 30 cm on a side holds 18 L of dielectric oil, which is composed of about 75% aliphatic hydrocarbons ($C_{10}H_{20}$-$C_{15}H_{28}$) and about 25% aromatic hydrocarbons (e.g. benzene and styrene) [27]. All experiments are performed at room temperature (~20°C). The working liquid has the following properties: mass density of 850 kg/m^3, kinematic viscosity of 4.3×10^{-6} m^2/s, conductivity of 1.15×10^{-9} S/m, and relative permittivity of 2.2. The tank is made of black plastic to absorb the laser reflection as much as possible.

An actuator (1) consisting of a stainless steel blade electrode ① and a plane electrode ② is submerged in this oil. The corners of the blade electrode are rounded to reduce edge effects. The blade with a length of 10 cm and a radius of curvature of 5 μm is fixed to the bottom of the tank lid. The plate with an area of 20 × 20 cm^2 is installed below and perpendicular to the blade. The electrode gap can be easily adjusted from 1 to 4 cm by turning the knob on the top of the lid. Negative DC voltages covering a wide range (0 to −40 kV) are applied to the blade and controlled by a Spellman SL1200 high voltage power supply. The current passing through the electrodes is recorded with a shunt resistor and an oscilloscope. Tracer particles of SiO_2 with a concentration of 0.01 g/L and a diameter of 0.5 μm are added. The laser beam (3) generated by

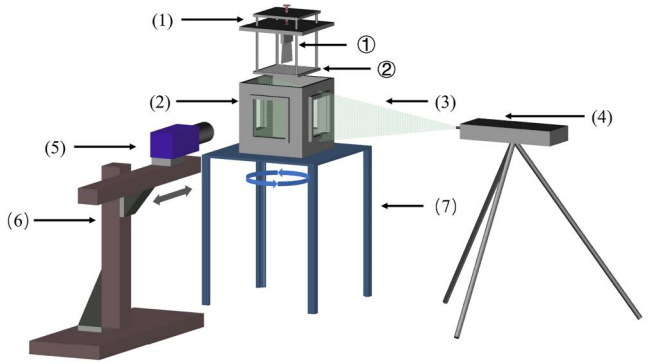

FIGURE 1 Experimental setup: (1)-EHD jet actuator, consisting of ①-blade electrode, ②-plane electrode, (2)-dielectric liquid container, (3)-laser beam, (4)-double pulse Nd:YAG laser, (5)-charge coupled device digital camera LaVision Imager pro X, (6)-camera displacement system, (7)-rotating available container support platform.

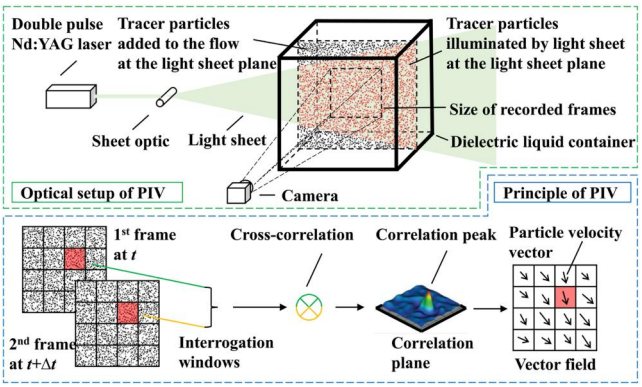

FIGURE 2 Schematic illustration of a 2D-PIV system and its velocity calculation principle.

an Nd:YAG laser (4) can illuminate the measurement plane at a frequency of 4 Hz through the window embedded in the tank wall. The DaVis algorithm for computing velocity vector fields is based on the detection of positional differences of exposed particles between two images illuminated by the double pulse laser [23]. A field-capturing charge coupled device (CCD) camera (5) with a spatial resolution of 2048 × 2048 pixels is placed normal to the laser plane. The camera displacement system (6) allows for near-field or far-field measurements. By rotating the tray above the support platform (7) by 90°, the blade electrode in the cell can face the camera with its plane surface or its side, which corresponds to the plane or profile measurement of the jet.

2.2 | Validity and reliability of PIV techniques

The objective of the first series of measurements is to verify proper operation of the system over the entire measurement range, that is, voltages between 0 and −40 kV and inter-electrode distances ranging from 1 to 4 cm. Due to the large number of tests and the fact that EHD flows produced by the blade-plane actuator are usually unsteady for instantaneous fields, a statistical analysis of the velocity data must first be made.

The PIV system is an optical instrument for flow visualisation and determination of the velocity distribution in fluids (see Figure 2). Two consecutive frames with a short interval Δt are recorded thanks to the motion of the light scattering particles following the fluid. This image pair can be divided into several small interrogation windows, to each of which a cross-correlation algorithm is applied to obtain a correlation plane. Here the correlation peak denotes the most likely destination position of the particle displacement, and then the particle velocity vector can be determined from the displacement estimation associated with the correlation peak and the known time difference Δt [28]. However, accurate measurements in temporal and spatial velocity fields necessitate that uncertainty quantification method be employed to investigate PIV error sources. These uncertainties may arise from inhomogeneous distribution of tracer particles, non-conformity of tracer particles with flow, out-of-plane displacement of particles, image distortion, pixelisation, illumination, background intensity and CCD noise [21, 29]. In our case, to record high quality frames in the whole velocity range, we should make the displacement of the seeding particles in the main jet region equal to about 10 pixels in each measurement. Therefore, an appropriate selection of Δt according to the specific conditions allows us to ensure this displacement [30] and to obtain a measurement precision of less than 1%. By adhering to this criterion, the statistical analysis of instantaneous samples in the main jet region should follow a Gaussian distribution.

Figure 3a,b show a comparison of velocity histograms for different interval Δt in the most intense pulsation case (the applied voltage $U = -30$ kV, and the inter-electrode distance $H = 1$ cm). Pre-tests have shown that $\Delta t = 100$ μs is usually valid for a moderate $\overline{E}_{app}$, which is an apparent mean electric field equal to the ratio of voltage to electrode gap. For instance, $\Delta t = 100$ μs applies to the case of $\overline{E}_{app} < 15$ kV/cm, where the bell-shaped velocity statistics curve representing the normal distribution holds. But in the case $\overline{E}_{app} = 30$ kV/cm, the jet has strong velocity fluctuations in the turbulent flow fields, and $\Delta t = 100$ μs becomes invalid.

The velocity statistics for $V_x = 0$ and $V_y = 0$ are displayed at the peak of the distribution in Figure 3a,b. For $\Delta t = 100$ μs, it is extremely implausible that these zero values appear at the location of the core region of the jet. In fact, when the algorithm fails to calculate the displacement of a particle over an interrogation window, a zero velocity is assigned to this point to represent the uncorrelated vector. This also indicates that the selection of $\Delta t = 100$ μs is inappropriate. Then, $\Delta t = 40$ μs proves to be suitable for $\overline{E}_{app} = 30$ kV/cm, where the histogram has a lower zero value bar, indicating fewer uncorrelated vectors. Similarly, the shorter bars located on the left side of the histogram indicate a lower probability of obtaining large amplitude velocities for $\Delta t = 100$ μs, resulting in a slightly right-skewed distribution. In view of the presence of a large number of zero values and the absence of high velocity samples, the time-averaged velocity for $\Delta t = 100$ μs is certainly underestimated.

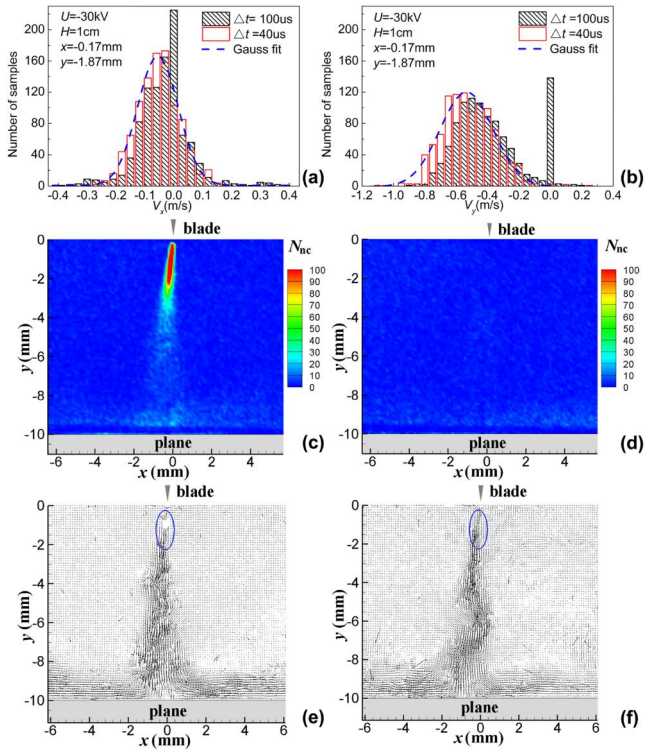

FIGURE 3 Statistical analysis of the time interval Δt for $U = -30$ kV, $H = 1$ cm based on 1000 samples. Histograms of (a) V_x, and (b) V_y at a point of the main jet region, with $\Delta t = 100$ μs for slash-filled black bars and $\Delta t = 40$ μs for hollow red bars. Distribution of the number of uncorrelated points N_{nc}, with (c) $\Delta t = 100$ μs, and (d) $\Delta t = 40$ μs. Instantaneous velocity vector fields, with (e) $\Delta t = 100$ μs, and (f) $\Delta t = 40$ μs.

However, when the interval is reduced to $\Delta t = 40$ μs, a standard normal distribution can be seen, indicating that the sampled instantaneous velocity at a given point is distributed with the same probability on both sides of the time-averaged value. We then extract all uncorrelated vectors among 1000 samples at each position of the velocity field for $\Delta t = 100$ μs (see Figure 3c), the uncorrelated points N_{nc}, which account for more than 10% of the total 1000 samples, are mainly located on the axis of the jet below the blade electrode. Intuitively, we thought that these uncorrelated points are due to the lack of seeding particles, which play a crucial role in evaluating the cross-correlation of the interrogation windows for each image pair. However, by examining the images, we confirmed that the number of particles per interrogation window is sufficient, that is, more than four particles are available for an interrogation window of 32 × 32 pixels.

If we move on to Figure 3e, the instantaneous velocity vector field might provide consistent evidence of an association between uncorrelated points and high velocity positions. Too high a velocity at the near blade region can lead to a displacement of seeding particles greater than the maximum distance permitted by the PIV algorithm within the time $\Delta t = 100$ μs. This is why none of the vectors appear near the electrode (see the vectorless region surrounded by the blue oval in Figure 3e). A verification of the above hypothesis requires the calculation of the theoretical travelling distance of the seeding particles. In our case ($\overline{E}_{app} = 30$ kV/cm), when the displacement evaluation is applied to an interrogation window of 32 × 32 pixels with an overlap of 50%, the preset interval $\Delta t = 100$ μs can give rise to a theoretical maximum displacement of 16 pixels for a tracer particle (equivalent to about 0.1 mm). Then, according to Figure 3b, a large number of high velocities V_y, which are missing in the left part of the histogram, should lie in the range of 0.7–1.1 m/s. V_y (0.7–1.1 m/s) multiplied by Δt (100 μs) yields a displacement of 0.07–0.11 mm, corresponding to approximate 12–18 pixels. This travelling distance is greater than the normal standard (8–10 pixels) and sometimes this value exceeds the maximum size (16 pixels in our case). As a result, particles with such velocities move out of the detection windows, which prevents the PIV analysis algorithms from correctly calculating their displacement. Only zero values can be assigned near the electrode region.

To address these problems, we attempt to keep the seeding particles within the interrogation window by reducing the interval Δt to 40 μs. In this way, the product of V_y (0.7–1.1 m/s) and Δt (40 μs) results in a displacement of 0.028–0.044 mm (5–8 pixels). The slash-filled black zero-velocity bar in Figure 3b is shifted to the left to fill the high velocity intervals of the histogram so that the hollow red bars follow a Gaussian distribution. It can be seen in Figure 3d that the number of uncorrelated images near the electrode is reduced from more than 200 to less than 20 after the adjustment. In summary, the choice of Δt remains delicate, it should be neither too large (which leads to a large number of uncorrelated points) nor too small (which causes a loss of measurement accuracy). Δt should be adjusted to achieve the optimal value for each measurement.

Once the selection of Δt is clarified, another important issue is to determine the minimum number of samples necessary for the calculation of the time-averaged flow field. For this, we have to investigate the convergence of the velocity at a certain point. Figure 4 presents an example of the evolution of $\overline{V}_i$ (black square symbols) and its uncertainty ΔV_i (red bars) at a point in the main jet region, where i represents the x-axis or y-axis in Cartesian coordinates. $\overline{V}_i$ is calculated from all n instantaneous velocities, and ΔV_i is calculated by $3\sigma_i/\sqrt{n-1}$ [31], where σ_i is the standard deviation of $\overline{V}_i$. Hence, the confidence level of velocity can reach 99.7% with $\overline{V}_i \pm \Delta V_i$ as the confidence interval.

In Figure 4, we have $\overline{V}_x = -3.9 \pm 1.42$ mm/s, and $V_y = -87.61 \pm 1.97$ mm/s when $n = 1000$. The velocity uncertainty decreases exponentially as the number of samples increases. $n \approx 700$ appears to be the threshold at which $\overline{V}_i$ is kept unchanged and ΔV_i converges to an asymptotic value. Following this experimental protocol, a series of preliminary tests are performed and $n = 1000$ proves to be valid for all PIV measurements in our case.

3 | RESULTS

3.1 | Selection of the electric field criterion

Upon acquiring all basic data of EHD jets, a primary concern is to discuss the range of velocities driven by electric fields, so

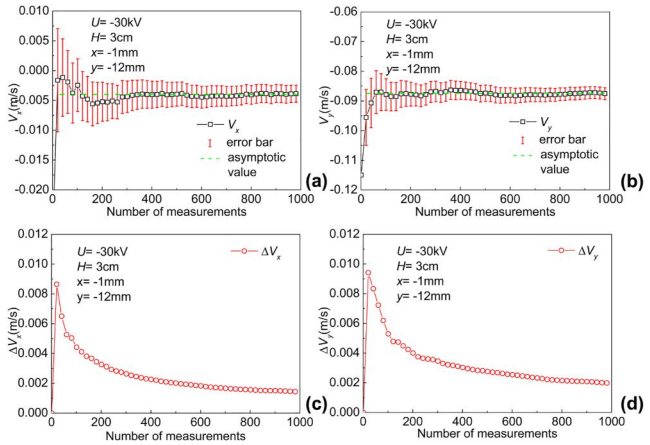

FIGURE 4 Evolution of the time-averaged velocity convergence (a) $\overline{V}_x$, (b) $\overline{V}_y$, and the velocity uncertainty convergence (c) ΔV_x, (d) ΔV_y with the number of samples at a point in the main jet region for $U = -30$ kV, $H = 3$ cm.

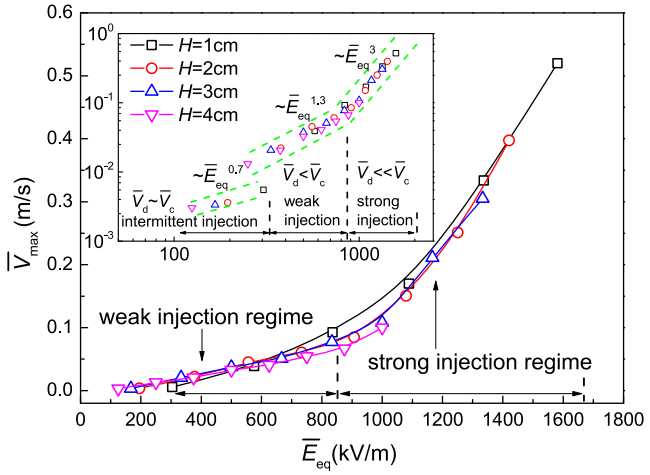

FIGURE 5 Variation of the maximum velocity $\overline{V}_{max}$ with applied electric field $\overline{E}_{eq}$ for different H.

it is necessary to select a uniform criterion related to the electric field (voltage or electric field strength).

Referring to [20] in which a linear V-U law at low voltages and a power growth of the velocity at high voltages are valid, we present a quantitative analysis of the V-E law, which allows us to consider both the role of applied voltage and electrode spacing in driving charged liquids. Previous studies have successfully demonstrated an evolutionary characteristic similar to the V-U law using the $\overline{V}_{max}$-$\overline{E}_{app}$ plot, where $\overline{V}_{max}$ is the maximum (centreline) velocity of the time-averaged flow field. In this plot, the low slope curve corresponds to the weak injection regime, followed by the high slope nonlinear curve associated with the strong injection regime [12]. However, in our blade-plane geometry, the overlapping of $\overline{V}_{max}$-$\overline{E}_{app}$ curves is true only for $H = 3$ cm and $H = 4$ cm, but invalid for $H = 1$ cm and $H = 2$ cm. This means that for $H = 1$ cm and $H = 4$ cm, very different $\overline{V}_{max}$ is obtained despite the same $\overline{E}_{app}$. In fact, $\overline{E}_{app}$, as the name implies, is adapted to uniform electric fields produced by symmetric electrode structures (e.g. the plane-plane geometry) rather than severe non-uniform electric fields generated by asymmetric electrode configurations (e.g. the blade-plane geometry). Therefore, inspired by [19], the concept of an equivalent mean electric field $\overline{E}_{eq}$ is proposed in this study to recalibrate the electric field so that the $\overline{V}_{max}$-$\overline{E}_{app}$ curves for all H have fully overlapping features. This applied electric field is given by

$$\overline{E}_{eq} = (|U|/H)^{\beta} = \overline{E}_{app}{}^{\beta} \quad (1)$$

where β is a modified exponent. Thus, we have to find how large to make β so as for the overlapping of all curves to hold. By superimposing the $\overline{V}_{max}$-$\overline{E}_{eq}$ curves of $H = 1$ cm and $H = 2$ cm on those of $H = 3$ cm and $H = 4$ cm (see Figure 5), β can be derived from Equation (1) reversely. Hence, we have $\beta = 1$ for $H = 3$ cm and $H = 4$ cm, $\beta = 0.96$ for $H = 2$ cm and $\beta = 0.92$ for $H = 1$ cm.

In addition to the weak injection regime with nearly linear growth and the strong injection regime with power growth observed in the linear-linear plot, a third regime can be distinguished in the log-log plot (see the small image in Figure 5, which is not easily detected on the linear scale due to its too small value of $\overline{V}_{max}$. We can see that the exponent of the power function for these three regimes gradually increase, and equals 0.7, 1.3 and 3 respectively. If we examine the flow field of the first regime that conforms to the law of $\overline{V}_{max} \sim \overline{E}_{eq}{}^{0.7}$, (corresponding to a set of PIV measurements at $U = -5$ kV), we find that the EHD jet in this regime exhibits intermittent injection characteristics, that is, the voltage is very close to the threshold voltage U_{th}, and the jet is extremely irregular and even disappears completely for considerable period of time [12]. It is usually believed that in isothermal fluids of low conductivity (not purely insulating liquids), conduction and injection can coexist. When a voltage is applied, one phenomenon overwhelms the other. Only in the transition regime from conduction to injection, the two modes coexist with similar weights [11]. This is exactly the phenomenon we observe in intermittent jets, where the flow under the blade tip is directed towards the counter-electrode due to the repulsion of injected charges (but the repulsion is not strong enough for the jet to reach the plane electrode, and the velocity disappears in the bulk due to viscous dissipation), while the fluid on both sides of the blade flows towards it under the conduction mechanism. In addition, the difference between the intermittent injection and the other two continuous injection regimes lies in the fact that as the electric field increases, $\overline{V}_{max}$ of the intermittent injection requires a 'jump' to enter the weak injection regime, while the velocity between weak and strong injection regimes is smooth and continuous.

When the diffusion velocity is neglected in EHD problems, the ion velocity with respect to the electrode usually contains two components, that is, the drift velocity and the convective velocity. It is interesting to compare the two components to see which one is more dominant [32]. Generally, the electric field and the flow velocity vary at different locations between the

electrodes. To assess the overall effect, we choose the equivalent mean electric $\overline{E}_{eq}$ and centreline mean velocity $\overline{V}_{y,c}$ (not plotted in this paper) to calculate the mean drift velocity $\overline{V}_d = \kappa \overline{E}_{eq}$ and the mean convective velocity $\overline{V}_c = \overline{V}_{y,c}$, where $\kappa = 1 \times 10^{-8}$ m^2/(V s) is the ion mobility [1, 16]. The plot of $\overline{V}_c/\overline{V}_d$ as a function of $\overline{E}_{eq}$ is shown in Figure 6. Similarly, three segments with different growth rates of $\overline{V}_c/\overline{V}_d$ are detected to distinguish the three regimes. The intermittent injection is characterised by $\overline{V}_c/\overline{V}_d \approx 1 \sim 2$, which means that neglecting the drift component is unreasonable over the entire range of intermittent jets (note that intermittent jets exist only in the vicinity of the blade electrode). This is different from the cases of EHD jets flowing through the whole electrode spacing under strong electric fields. In these cases, the presence of self-similar regions away from the active electrode allows analytical or semi-empirical models to consider only the convective term of the current density, since the drift velocity is usually much smaller than the convective velocity [33]. The comparable amplitude of these two velocity components also causes $\overline{V}_c/\overline{V}_d$ to undergo a 'jump' into the weak injection regime. Then, the slope of $\overline{V}_c/\overline{V}_d$ gradually increases with $\overline{V}_c/\overline{V}_d \approx 2 \sim 8$ for the weak injection, and $\overline{V}_c/\overline{V}_d > 8$ for the strong injection.

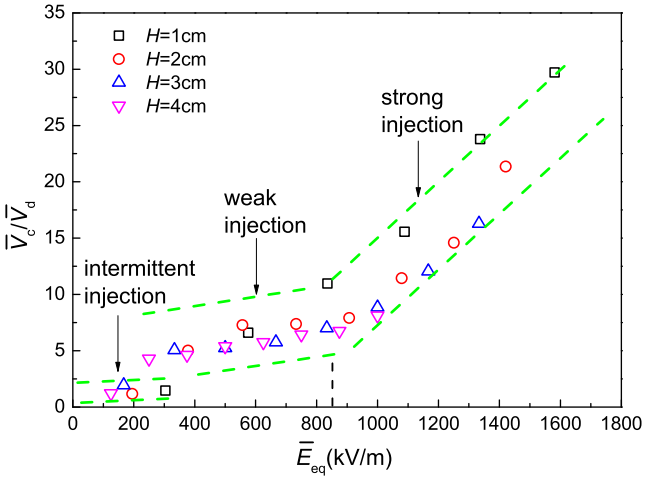

FIGURE 6 Variation of the ratio of convective velocity to drift velocity $\overline{V}_c/\overline{V}_d$ with applied electric field $\overline{E}_{eq}$ for different H.

3.2 | Parametric study of EHD jets

In this section, the characteristic data of EHD jets are analysed and a database is established through a comparative investigation with classical jets and thermal plumes, including axial velocity evolution, maximum velocity position, half-width evolution and axial turbulence intensity evolution. Several parameters used for characterising thermal plumes and classical jets are listed in Table 1.

3.2.1 | Characteristics of the axial velocity

There exists a rapid decrease in the axial mean velocity in the self-similar region for classical jets and thermal plumes (excluding round plumes), which is similar to the axial velocity evolution of EHD jets. Therefore, referring to the equation reported in ref. [36], the expression for the axial velocity can be written as

$$\overline{V}_{y,c}/\overline{V}_{y,max} = \left[K_u\left(y - y_{max}\right)/H\right]^{\alpha} \quad (2)$$

where $\overline{V}_{y,c}/\overline{V}_{y,max}$ is the dimensionless axial velocity equal to the ratio of the local centreline velocity to the maximum axial velocity in the time-averaged flow field. K_u is the decay rate of $\overline{V}_{y,c}$, y_{max} is the position of $\overline{V}_{y,max}$. α is the exponent in Equation (2) which determines the extent to which $\overline{V}_{y,c}$ decays in the self-similar region and thus the ability to maintain momentum.

Figure 7 presents the evolution of α versus $\overline{E}_{eq}$ for different H. All α lie in the range of $-0.5 \sim 0$, corresponding to the coefficients between plane thermal plumes and plane jets (see Table 1). This finding suggests that the ability of two-dimensional EHD jets to hold their velocities is much greater than that of classical plane jets but not as good as that of plane thermal plumes. The most likely reason is as follows. After ejection from the nozzle, a classical jet subjected to viscous friction can only move downstream via inertia effect, leading to a sharp drop of axial velocity. In contrast to the classical jet, a thermal plume has enough extra force at origin to maintain its velocity. Compared with the former two, the Coulomb force of an EHD jet contributes to the acceleration of the charged fluid near the blade electrode, but the range of the electric force is far smaller than that of the buoyant force of the thermal plume. As a result, the EHD jet bears a resemblance to both plane jets and plane thermal plumes.

The distance-independent feature of α is much more evident for higher $\overline{E}_{eq}$, where all values tend to $\alpha \approx -0.22$. This is probably because for high $\overline{E}_{eq}$, the more stable charge injection results in a similarity in momentum evolution, which is affected by the combination of EHD acceleration and viscous dissipation. Nevertheless, in Figure 7, the distribution of α is more dispersed in the range of low $\overline{E}_{eq}$, and the smaller the electrode gap, the larger the α possessed by the jet. Since the axial electric field decreases rapidly with distance (it mainly follows the $E \sim 1/y$ law without space charge and there is also a small logarithmic dependence), and its distribution near the blade area appears to be less dependent on H at a fixed voltage (e.g. $U = -10$ kV), the electric force acting on space charges would make the position y_{max} at $H = 1$ cm approximately equal to y_{max} at the other H. Thus, when normalised by H, y_{max}/H at $H = 1$ cm is the largest among all electrode spacings (see Figure 8), indicating a longer relative acceleration distance and therefore a better ability to maintain the axial velocity (α close to zero) under the action of the electric force. This velocity field is similar to that of the thermal plume.

Figure 8 provides the position statistics for the maximum velocity y_{max}/H. Each curve seems to have its own peak in the range of $\overline{E}_{eq}$ corresponding to the weak injection regime in Figure 5. In the initial part of the curve, y_{max}/H increases with

TABLE 1 Characteristic parameters of thermal plumes and classical jets

Parameters	Criterion coefficient	Patten	Configuration	
			Blade-plane	Needle-plane
Axial velocity	Decay exponent α	Plume	0 [34]	−0.33 [35]
		Jet	−0.5 [36]	−1 [37]
Half-width	Growth rate K_y	Plume	/	0.14–0.18 [38]
		Jet	0.09–0.14 [36]	0.075–0.09 [39]
Axial turbulence intensity	Constant in self-similar zone $I_{y,c}$	Plume	/	0.22 [28]
		Jet	0.2–0.3 [36]	0.2–0.25 [37]

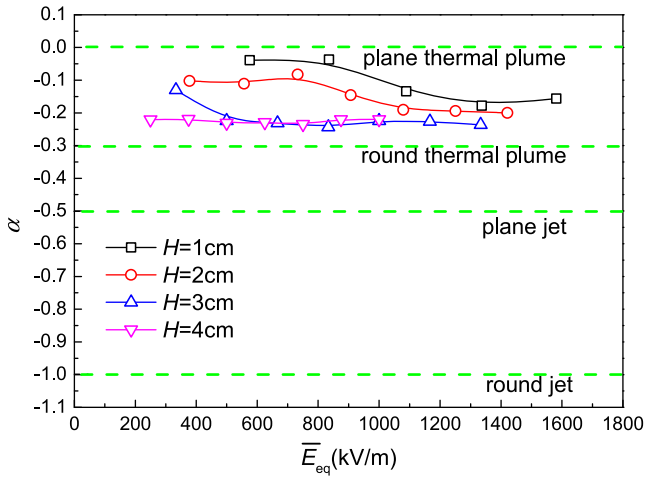

FIGURE 7 Variation of the exponent α with applied electric field $\overline{E}_{eq}$ for different H in the self-similar zone.

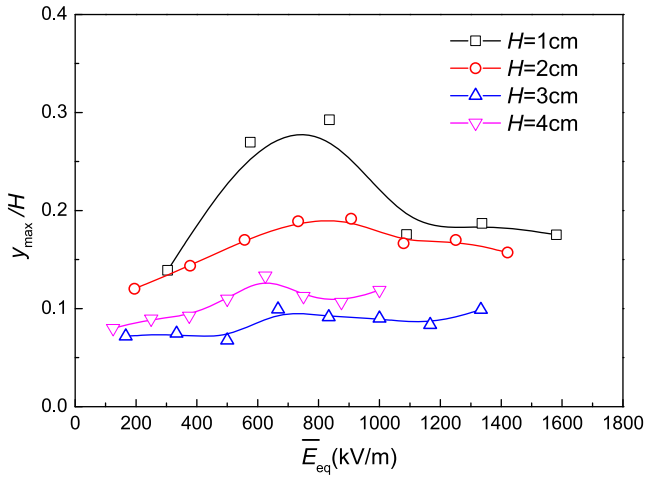

FIGURE 8 Variation of the maximum velocity position y_{max} with applied electric field $\overline{E}_{eq}$ for different H.

$\overline{E}_{eq}$ as the increase in kinetic energy causes the jet to accelerate further. However, y_{max}/H decreases with $\overline{E}_{eq}$ at the end of the curve. This is because the higher velocity results in the larger pressure gradient, which decelerates the jet in the impinging zone. Considering the similarity of the momentum evolution resulting from the combined mechanism of acceleration by electric force and deceleration by pressure, one can predict that at larger $\overline{E}_{eq}$ all curves converge to $y_{max}/H \approx 0.14$. Note that tests under larger $\overline{E}_{eq}$ were not conducted in order to prevent dielectric breakdown (e.g. $U = -40$ kV, $H = 1$ cm).

3.2.2 | Spreading rate of the half-width

The thickness of the jet gradually widens with distance when the jet spreads into the dielectric liquid (see Figure 14e). The half-width $x_{1/2}$ is generally defined as the normal distance between the axis of the jet and the contour of the dimensionless velocity $\overline{V}_y/\overline{V}_{y,c} = 0.5$. Taking into account the linear properties of the thickening of the jet [36, 37] and the description of EHD plume model in ref. [19], the half-width of the EHD jet is given by

$$x_{1/2}/H = K_y(y - y_0)/H \tag{3}$$

where y_0 is a virtual origin at which the jet stops contracting and starts expanding [12], K_y is the spreading rate. A larger K_y is indicative of more entrainment of fluid in the main jet region. We can see in Figure 9 that K_y decreases with $\overline{E}_{eq}$ for all H. In fact, at low $\overline{E}_{eq}$, the charge injection is unstable and weak, and the instantaneous jet does not flow strictly along the centreline (y-axis). The jet also takes more time to mix with the surrounding medium. Therefore, the jet in the time-averaged flow field is much wider due to the increase in the velocity ratio of $\overline{V}_x/\overline{V}_y$.

The K_y of the EHD jet covers a wide range between 0.1 and 0.35, which is more widely distributed than that of classical jets and thermal plumes. The latter two range from 0.075 to 0.14 and 0.14–0.18 respectively (see Table 1). Therefore, we can conclude that EHD jets expand much faster than thermal plumes and classical jets in the range of $\overline{E}_{eq}$ corresponding to nearly the weak charge injection. When $\overline{E}_{eq}$ reaches the value corresponding to the strong injection regime, the EHD jets begin to behave as thermal plumes. And at higher $\overline{E}_{eq}$, they have similar values of K_y as the classical jets. Therefore, the electric field-controlled EHD jets have a larger range of K_y than classical jets and thermal plumes, which implies that EHD pumping technologies have more flexible regulation in the field of flow control.

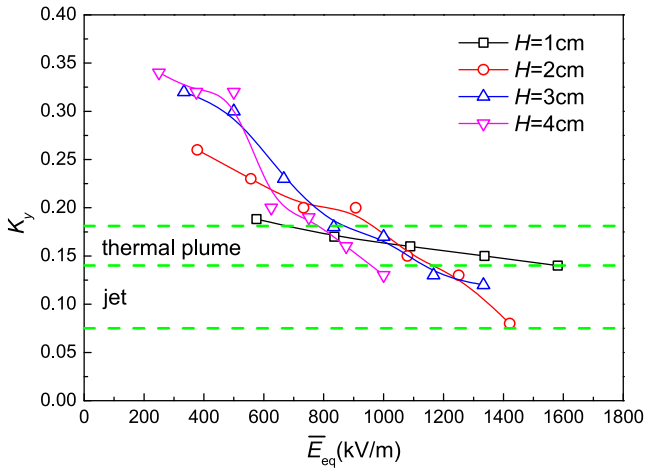

FIGURE 9 Variation of the spreading rate K_y with applied electric field $\overline{E}_{eq}$ for different H.

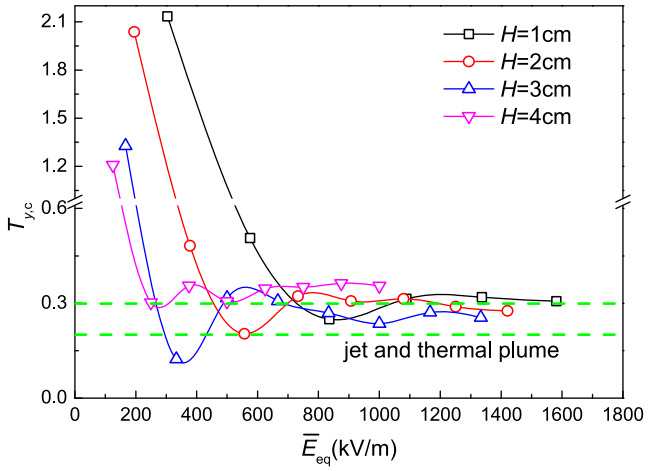

FIGURE 10 Variations of the axial turbulence intensity $T_{y,c}$ with applied electric field $\overline{E}_{eq}$ for different H.

3.2.3 | Variation of the axial turbulence intensity

For classical jets, a larger root mean square (RMS) of the velocity indicates a higher level of pulsation. The RMS of the velocity $v_{y,\mathrm{rms}}$ is defined as

$$v_{y,\mathrm{rms}} = \sqrt{\frac{1}{n}\sum_{k=1}^{n}\left(v'_{y,k}\right)^2} \tag{4}$$

where $v'_{y,k}$ is a randomly varying perturbation of velocity at any point in a turbulent jet at the kth measurement. $v'_{y,k}$ equals the instantaneous velocity minus the corresponding time-averaged velocity [12]. The turbulence intensity in the centreline of the self-similar region is written as

$$T_{y,\mathrm{c}} = v_{y,\mathrm{c,rms}}/\overline{V}_{y,\mathrm{c}} \tag{5}$$

where $v_{y,\mathrm{c,rms}}$ and $\overline{V}_{y,\mathrm{c}}$ are the $v_{y,\mathrm{rms}}$ and $\overline{V}_y$ on the centreline respectively. Figure 10 plots the evolution of $T_{y,\mathrm{c}}$ versus $\overline{E}_{eq}$ for all H. Most strikingly, at the low $\overline{E}_{eq}$ corresponding to the intermittent injection ($U = -5$ kV), $T_{y,\mathrm{c}}$ is greater than 100%, and such strong turbulence means that the velocity pulsation is of the same or even larger magnitude than the time-averaged velocity. As mentioned above, at $U = -5$ kV (which is close to the threshold of charge injection), the EHD jet is intermittent and unstable, with relatively large velocity pulsation $v_{y,\mathrm{c,rms}}$ despite the low $\overline{V}_{y,\mathrm{c}}$. However, this low kinetic jet is not associated with the laminar regime but with the turbulent regime. For the high $\overline{E}_{eq}$ in the strong injection regime, $T_{y,\mathrm{c}}$ remains almost unchanged and lies within the range of jets and thermal plumes. The minimum $T_{y,\mathrm{c}}$ for each H falls in the range of $\overline{E}_{eq}$ related to the weak injection regime, where a stable periodic oscillation of the instantaneous flow field is recorded and a wider jet with two rotating vortices in the time-averaged field is obtained compared to the highly unstable intermittent jet [12]. In this regime, the increase in $v_{y,\mathrm{c,rms}}$ is much smaller than the increase in $\overline{V}_{y,\mathrm{c}}$, resulting in a minimum turbulence intensity.

4 | DISCUSSION

4.1 | Effect of the charge recombination

The issue of unipolar injection into an insulating fluid has been well investigated in refs. [10, 18, 25, 33]. In these studies, dielectric liquids have extremely poor conductivity, which allows us to safely neglect the source term of the charge conservation equation, since the dissociation/recombination of impurities in the bulk is very weak and the two rates cancel each other out. Although this study also addresses electro-convecitve problems including unipolar injection, the high conductivity of 1.15×10^{-9} S/m in our liquid may necessitate considering both charge dissociation (the Wien effect) and charge injection mechanisms. The contribution of these mechanisms to the current can be demonstrated by analysing the current-electric field characteristics [40]. Moreover, the charge evolution in non-conducting dielectric liquids is generally determined by Coulomb repulsion and convection, while in our liquid with relatively large conductivity, the reduction of the space charge density under the charge recombination effect needs to be considered. An analysis of the recombination length seems to be appropriate.

4.1.1 | Current-electric field characteristics

Figure 11 presents the I_t-$\overline{E}_{eq}$ curve for various H. The current I_t (in the form of line density in our 2D case) grows almost linearly with the electric field, although there is a less obvious non-linear variation in the strong injection regime. In the log-log plot (see the small image at the top in Figure 11), it can be seen that the EHD jet roughly follows the law of $I_t \sim \overline{E}_{eq}^{\,1}$, $I_t \sim \overline{E}_{eq}^{\,1.1}$, and $I_t \sim \overline{E}_{eq}^{\,1.4}$, corresponding to the three regimes of Figure 5, respectively. This indicates that the conduction current accounts for a very large proportion of the total

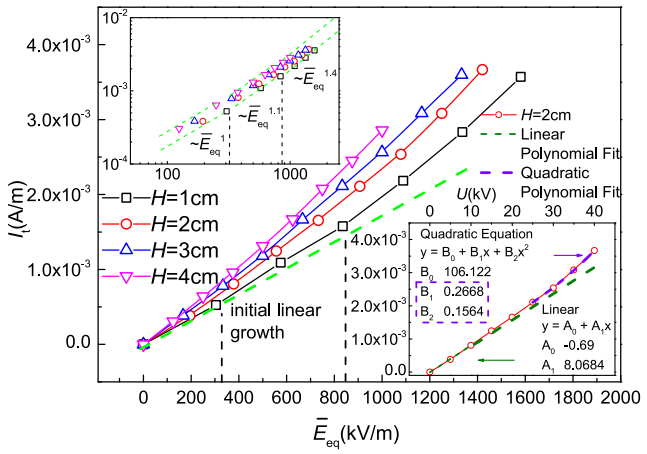

FIGURE 11 Total Electric current I_t versus applied electric field $\bar{E}_{eq}$ for different H.

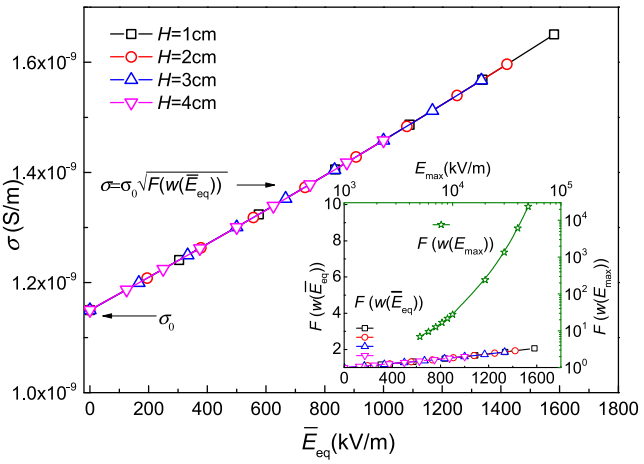

FIGURE 12 Variations of the conductivity σ with applied electric field $\bar{E}_{eq}$ for different H.

current (equal to the sum of the conduction current and the injection current [12]) over the entire applied electric field range, although the injection current increases continuously with the electric field.

It is well known that in dielectric liquid with low conductivity, a quadratic dependence of I on U is valid for high applied voltages, which is associated with the injection current [10, 41]. In order to verify the existence of the injection current in our case, we take $H = 2$ as an example and plot the I-U curve to make a comparative analysis in the same physical situation. In the I-U curve (see the small image at the bottom in Figure 11, a perfect ohmic-dependent current holds true in the range of low voltages related to the intermittent injection regime and a part of the weak injection regime through the linear polynomial fit, which indicates that the injection current in this regime is very small. For the high voltages corresponding to the strong injection ($U \geq 25$ kV for $H = 2$), a quadratic polynomial fits the I-U curve fairly well [23], with a ratio of the coefficient B_1 (whose term represents the conduction current) to B_2 (whose term represents the injection current) being approximately 1.7, thus verifying the presence of the injection current.

In addition to the high proportion of conduction current at relatively high conductivity, the electrode material also determines the profile of the I-E curve. The metal work function of the electrode material determines the minimum energy required to transfer an electron from the inside of the electrode to the outside, and its magnitude is inversely proportional to the current in the dielectric [42]. In our work, we use stainless steel as the electrode material, which has a high work function (4.48 ~ 5.05 eV) in metals. The less evident non-linear I_t-$\bar{E}_{eq}$ curve is in accordance with that of the stainless steel electrode reported in ref. [42]. Such a high work function of the stainless steel electrode can be interpreted by the surface morphology of the electrodes. According to Wu et al. [43], the stainless steel electrode has a shallow surface feature in metals with a roughness amplitude of only 26.91 nm, which may result in a less prominent space charge injection capability among all metallic materials.

For the same $\bar{E}_{eq}$, I_t is greater with large H than that with small H. This feature is consistent with the I-E curve in ref. [42] and can be explained by the electron impact ionisation process, whose theory suggests that the logarithm of I is proportional to the distance H [42]. In fact, pre-existing micro bubbles, localised internal vaporisation, molecular decomposition and mechanical movement can largely lower the ionisation threshold and create a relatively low-density region with a long mean free path and an intense electric field near the electrode, allowing the free electrons to accelerate before being rapidly trapped by the liquid molecules [44]. In addition, the study in ref. [23] also found that when H is greater than a certain value, the I-E curves tend to superimpose on each other.

4.1.2 | Electric field-dependent conductivity

Under the action of an external electric field, the dissociation effect of impurities in dielectric liquids with conductivity ranging from 10^{-11} to 10^{-7} S/m is enhanced [2], breaking the dynamic equilibrium between dissociation and recombination that was previously achieved in the absence of an electric field [45]. This can be demonstrated by the electric field-dependent conductivity equation associated with the Wien effect [16, 40].

$$\sigma = \sigma_0 \sqrt{F(w(E))} \tag{6}$$

where σ_0 is the initial conductivity, $F(w(E)) = I_1(4w)/(2w)$ is the Onsager function acting as the relative intensification of dissociation, with I_1 being the modified Bessel function of the first kind and order 1. $w(E)$ is the ratio of the Bjerrum distance to the Onsager distance, in which E is the electric field strength.

Figure 12 shows the variation of σ with $\bar{E}_{eq}$. σ increases almost linearly from 1.15×10^{-9} S/m without initial electric field to 1.65×10^{-9} S/m when $\bar{E}_{eq} \approx 1500$ kV/m. Since the variable substituted into the conductivity equation is the equivalent mean electric field $\bar{E}_{eq}$ adapted to this study, σ

reflects only the effect of the overall change in the conductivity of the liquid. In contrast, the enhanced dissociation effect is more pronounced for strong electric fields (much larger than $\overline{E}_{eq}$) in the vicinity of the blade electrode. To compare the increase rate of dissociation intensity near the electrode with that of the overall liquid, we plot both $F(w(\overline{E}_{eq}))$ and $F(w(E_{max}))$ in the same graph (see the small image in Figure 12). Suppose that the maximum electric field near the electrode tip varies in the range from 5×10^6 V/m to 5×10^7 V/m [46], then the dissociation intensity factor $F(w(E_{max}))$ increases from 7 to more than 23,000 at this location. This reveals that despite the small area near the electrode tip, both sources of charge injection and enhanced dissociation need to be considered under conditions of strong electric field and relatively high electrical conductivity. However, in the bulk of the liquid, $F(w(\overline{E}_{eq}))$ of the liquid only changes from 1 to approximately 2.1.

4.1.3 | Characteristic length of the charge recombination

In non-conductivity liquids, the charge density decreases on the characteristic lines (the charge carrier trajectories) in the core region of the jet and follows the algebraic law $q = q_0/(1 + t/\tau_q)$ with $\tau_q = \varepsilon/\kappa q_0$, where q_0 is the uniform charge density on the injector, τ_q is the typical charge relaxation time related to Coulomb repulsion and convection effects [10]. However, in this study, the charge decay effect caused by the charge recombination mechanism, which follows the exponential decay law of charge relaxation $q = q_0 e^{-t/\tau}$ with $\tau = \varepsilon/\sigma$ should also be taken into account. Accordingly, the recombination length can be written as

$$L_r = \overline{V}_{ion}\tau \tag{7}$$

where $\overline{V}_{ion} = \overline{V}_c + \overline{V}_d$ is the velocity of ions that we mentioned in Section 3.1, In most cases, $\overline{V}_c \gg \overline{V}_d$. Only in the intermittent injection regime ($U_{int} = -5$ kV), the two components are of the same order of magnitude in our study. $\tau = \varepsilon/(\sigma_0\sqrt{F(w(E))})$ is the typical recombination time considering the field-enhanced dissociation effect. L_r is the characteristic distance that ions travel with drift and convective velocity before recombining (here we choose the mean velocity to represent the overall effect). Along the centreline of the jet, the charge density decays exponentially and reaches $1/e$ of the initial value at a distance of L_r from the tip of the blade electrode.

Figure 13 shows the evolution of the dimensionless length L_r/H as a function of $\overline{E}_{eq}$ for all H. Although τ decreases with $\overline{E}_{eq}$ (consider $\tau \sim 1/\sigma$ and see Figure 12), the increase of velocity with $\overline{E}_{eq}$ is even greater, so L_r/H still increases with $\overline{E}_{eq}$. In Figure 13, $L_r/H < 1$ is valid for all cases. This indicates that ions cannot move to the counter electrode within the recombination time, proving that the recombination process is relevant for all cases. The larger the electric field $\overline{E}_{eq}$, the slower the rate of decrease of the charge density along the jet axis based on the recombination mechanism.

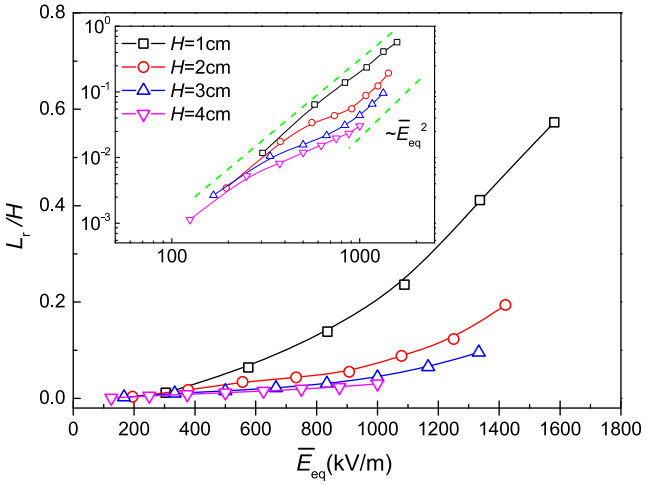

FIGURE 13 Variation of the dimensionless recombination length L_r/H with applied electric field $\overline{E}_{eq}$ for different H.

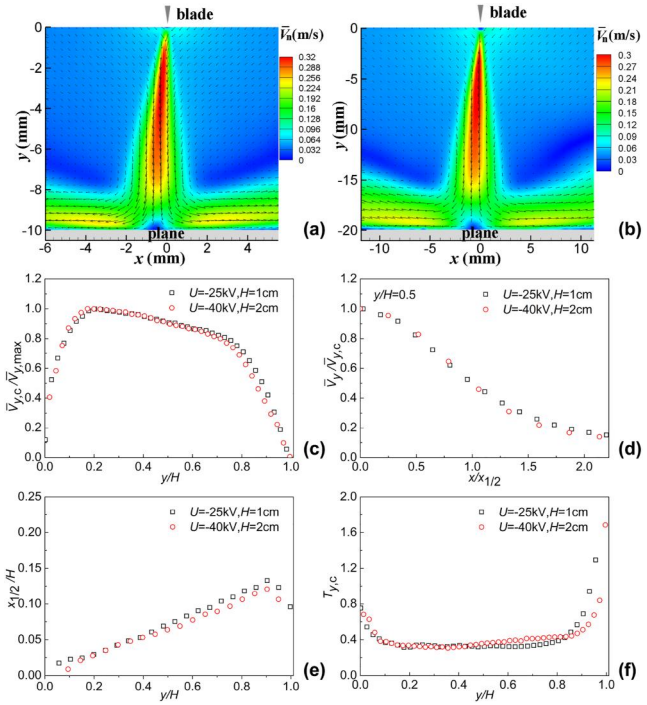

FIGURE 14 Similarity in flow structures and profiles of electrohydrodynamic (EHD) jets subjected to $\overline{E}_{eq}$ = 1333 kV/m. Velocity modulus $\overline{V}_n$ (m/s) and vector field for (a) $U = -25$ kV, $H = 1$ cm, (b) $U = -40$ kV, $H = 2$ cm, (c) evolution of the axial velocity, (d) velocity profile of $\overline{V}_y$ at the cross section $y/H = 0.5$, (e) evolution of the half-width, (f) variation of the axial turbulence intensity.

In the log-log plot (see the small image in Figure 13), the law of $L_r/H \sim \overline{E}_{eq}^{\ 2}$ is followed for all cases except for the weak injection regime that serves as a transition joining the other two regimes. In the strong injection regime, four electrode gap-dependent L_r/H-$\overline{E}_{eq}$ curves are distributed in parallel. The smaller the electrode spacing H, the larger the recombination length L_r/H, and the less the charge density reduction. In the intermittent injection regime, L_r/H-$\overline{E}_{eq}$ curve seems to be

independent of H. The above description can be interpreted from two perspectives. From a physical point of view, the structure of the time-averaged flow in the strong injection regime is a more stable impinging jet, and similar features can be observed under the same $\overline{E}_{eq}$ despite the different H. Therefore, neither $\overline{V}_{ion}$ nor L_r makes much difference for all H, resulting in L_r/H being inversely proportional to H. In the intermittent injection regime, the jet disappears in the bulk without arriving at the plane electrode. The electric field strength is weaker in this regime, and the pressure gradient along the axis of the plate has a significant effect on the velocity of the jet. The jet at smaller H is subjected to a larger pressure gradient at the same distance, which yields a smaller velocity $\overline{V}_{ion}$ and L_r. Hence, L_r seems to be proportional to H, and L_r/H is certainly independent of H. From a mathematical perspective, in the strong injection regime, taking $\overline{V}_{ion} \approx \overline{V}_c \sim \overline{E}_{eq}^{\ 3}$ (see Figure 5), and $\tau = \varepsilon/\sigma \sim \overline{E}_{eq}^{\ -1}$ (see Figure 12), we have $L_r/H \sim \overline{E}_{eq}^{\ 2}/H$. In the intermittent injection regime, given that $\overline{V}_c$ and $\overline{V}_d$ are of the same order of magnitude (see Figure 6), we assume that $\overline{V}_c \approx \overline{V}_d$, and thus we get $\overline{V}_{ion} \approx 2\overline{V}_d \sim \overline{E}_{eq}^{\ 1}$. At low $\overline{E}_{eq}$, σ is close to σ_0 (see Figure 12), so we assume $\tau \approx \varepsilon/\sigma_0 \sim \overline{E}_{eq}^{\ 0}$. In the log-log plot of Figure 13, L_r in the intermittent injection regime corresponds to $U_{int} = -5$ kV for all H, and at such a low $\overline{E}_{eq}$, we assume $\overline{E}_{eq} \approx |U_{int}|/H$. Finally, we get $L_r/H \sim \overline{E}_{eq}^{\ 1}/H \sim \overline{E}_{eq}^{\ 2}/|U_{int}|$.

4.2 | Similarity in flow structures

We now proceed to verify whether $\overline{E}_{eq}$ holds true for all flow field characteristics, not just $\overline{V}_{max}$, that is, for two cases with the same $\overline{E}_{eq}$, the jets should have similarities in terms of the time-averaged velocity fields, axial and lateral velocity profiles, half-width, and axial turbulence intensities. We recalculate the voltage corresponding to $\overline{E}_{eq}$ according to Equation (1), and present them in Table 2.

Ideally, a comparison should be made between the EHD characteristics of the same row of voltages in Table 2. To verifier the validity of $\overline{E}_{eq}$ for $H = 1$ cm and $H = 2$ cm (the similarity between $H = 3$ and $H = 4$ has been demonstrated in [12]), we choose the highest non-uniform electric field $\overline{E}_{eq} = 1333.3$ kV/m, which roughly corresponds to $U = -25$ kV and $U = -40$ kV for $H = 1$ cm and $H = 2$ cm, respectively.

Figure 14a,b show the time-averaged velocity fields for two selected cases, each jet moves downstream and gradually spreads before impinging normally on the plane electrode. Finally, two symmetrical wall jets are formed for each jet. The velocity distributions of the tow cases are significantly similar in the whole flow field.

To be more specific, the axial velocity for each case in Figure 14c increases to $y/H = 0.1$ and gradually decreases to $y/H = 0.7$, followed by a dramatic drop due to the impact. In Figure 14d, each lateral velocity profile in the self-similar region shows a Gaussian distribution (only the half-plane profiles are shown due to symmetry). A linear growth of the half-width

TABLE 2 Applied voltages corresponding to $\overline{E}_{eq}$ for all H

	U(kV)			
$\overline{E}_{eq}$ (kV/m)	1 cm $\beta = 0.92$	2 cm $\beta = 0.96$	3 cm $\beta = 1$	4 cm $\beta = 1$
166.7	−2.6	−4.2	−5	−6.7
333.3	−5.5	−8.8	−10	−13.3
500	−8.6	−13.4	−15	−20
666.7	−11.7	−18.1	−20	−26.7
833.3	−14.9	−22.9	−25	−33.3
1000	−18.2	−27.7	−30	−40
1166.7	−21.6	−32.5	−35	−46.7
1333.3	−24.9	−37.4	−40	−53.3

is presented for each case in Figure 14e. In terms of axial turbulence intensity in Figure 14f, a bathtub-like curve is plotted, where $T_{y,c}$ is very large near the blade electrode resulting from injection instability and even lager near the plane electrode due to the impact and reflection. In the self-similar region, $T_{y,c}$ is approximately equal to 0.32.

For all axial features, two curves in each plot are almost superimposed on each other, proving the validity of the $\overline{E}_{eq}$ criterion. These superimposed features are also valid for other cases such as $\overline{E}_{eq} = 833$ kV/m and $\overline{E}_{eq} = 1000$ kV/m. In summary, $\overline{E}_{eq}$ functions as an appropriate reference for determining the electric field in the blade-plane geometry.

The analysis of the different parameters (especially the axial features) demonstrates that the EHD jet can be divided into four zones. In Figure 15 we plot the axial velocity, half-width, momentum flux and axial turbulence intensity for $U = -30$ kV, $H = 3$ cm in the same graph for better comparison. In the region named acceleration zone 1, the axial velocity $\overline{V}_{y,c}/\overline{V}_{y,max}$ increases steeply and reaches a maximum at the end of the region. This increase is analogous to a thermal plume under the action of external forces. For the EHD jet, the electric force appears to be more intense in amplitude, but its range is much shorter compared to the buoyancy of the thermal plume. The same trend can be observed for the momentum flux $\dot{m}/\dot{m}_{max}$, In a continuous medium, the region below the electrode will be filled with the surrounding fluid due to the pressure difference during the fluid motion at the origin. As a result, the jet in zone 1 undergoes contraction, leading to a decrease in half-width $x_{1/2}/H$ at the beginning of zone 1. A high axial turbulence intensity $T_{y,c}$ is also evident because of the strong instability of charge injection and interaction with surrounding charges under strong electric fields. The zone 2 is a transition region characterised by the decrease in $\overline{V}_y$ and $T_{y,c}$. The length of this region is altered according to specific conditions. The zone 3 is a self-similar region where many studies have been performed for the parametric analysis of the jet structure. The decreasing $\overline{V}_{y,c}/\overline{V}_{y,max}$, linearly increasing $x_{1/2}/H$, invariant $T_{y,c}$ and $\dot{m}/\dot{m}_{max}$ are considered as general characteristics of this region. In the zone 4, the sudden rise in $T_{y,c}$ and the significant

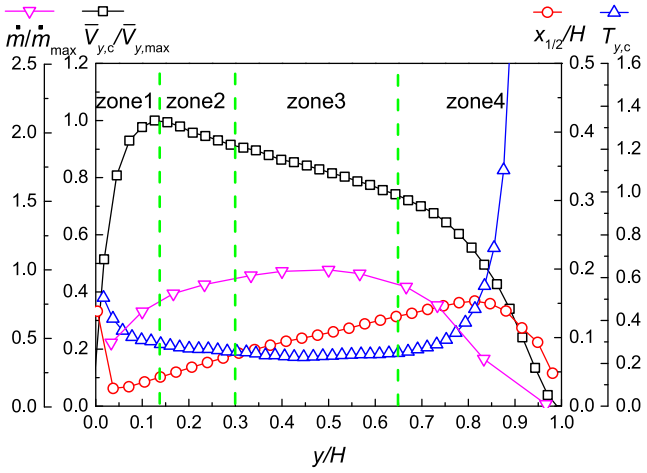

FIGURE 15 Variations of the axial characteristics with dimensionless distance y/H for $U = -30$ kV, $H = 3$ cm.

decrease in $\overline{V}_{y,c}/\overline{V}_{y,max}$ are the key features for detecting the initial position of this region.

5 | CONCLUSION

The main goal of the current study is to provide quantitative insight into the overall EHD jet structures in a blade-plane geometry. Based on a set of PIV measurements of velocity fields, a comparative analysis of EHD jets with classical jets and thermal plumes was made to distinguish their structural characteristics. The different flow patterns corresponding to various flow regimes of the EHD jets emphasise the need for a preliminary statistical analysis when making accurate measurements. Under the most extreme condition ($U = -30$ kV, $H = 1$ cm), the choice of $\Delta t = 40$ μs seems to be effective in correctly detecting the displacements of the particles in interrogation windows. The selection of 1000 samples also ensures the reliability of the time-averaged flow field measurements within the confidence interval.

The equivalent electric field criterion $\overline{E}_{eq}$ was proposed as a reliable reference for analysing the V-E characteristic in the blade-plane configuration. This allows us to distinguish the flow regimes and to find the structural similarities in the same physical situation. In the log-log plots of the $\overline{V}_{max}$-$\overline{E}_{eq}$ curves, three injection regimes conforming to the power function are clearly distinguished according to the gradual increase of the exponent. In the strong injection regime at high $\overline{E}_{eq}$, the convective velocity of ions is much greater than the drift velocity, while in the intermittent injection regime at low $\overline{E}_{eq}$, the former is comparable to the latter. The velocity undergoes a 'jump' from the intermittent injection to the weak injection, with the latter serving as a transition between the other two regimes. In the I_t-$\overline{E}_{eq}$ curve, a nearly linear increasing law proves that the conduction current accounts for a large proportion of the total current. The presence of the injection current was verified by fitting the I-U curve in the strong injection regime with a quadratic polynomial. The recombination length was discussed to evaluate the extent to which the charge density decreases along the jet axis due to the charge recombination effect. A law of $L_r/H \sim \overline{E}_{eq}^{\ 2}$ was identified for all cases, demonstrating that the larger the electric field and the smaller the electrode spacing, the less pronounced the decrease in charge density caused by charge recombination.

Parametric investigations of EHD jets show that the decay rate of the axial velocity in the self-similar region falls between that of plane jets and plane thermal plumes, which indicates that the ability of EHD jets to keep their kinetic energy is better than that of classical jets but inferior to that of thermal plumes. The EHD jet has a larger spreading rate and higher turbulence intensity at low $\overline{E}_{eq}$. These two parameters lie approximately in the range of plane jets and plane thermal plumes at high $\overline{E}_{eq}$. The similarities of flow field structures and parameters at the same $\overline{E}_{eq}$ are compared through case studies to verify the correctness of applying $\overline{E}_{eq}$ as a criterion. Based on the axial profiles including axial velocity, half-width, momentum flux and axial turbulence intensity, the EHD jet can be divided into four regions. Among them, the self-similar zone is the most important region with significant features.

ACKNOWLEDGEMENTS

This work was supported by the National Natural Science Foundation of China (51907118).

CONFLICT OF INTEREST

The authors declare that they have no known competing financial interests or personal relationships that could have appeared to influence the work reported in this study.

DATA AVAILABILITY STATEMENT

The data that support the findings of this study are available from the corresponding author upon reasonable request.

ORCID

Zelu Yan https://orcid.org/0000-0002-0857-3140

REFERENCES

1. Xue, Q., et al.: Mobility of charge carriers in mineral oil and ester fluids. High Volt. 6(6), 1040–1050 (2021)
2. Vázquez, P.A., et al.: In-depth description of electrohydrodynamic conduction pumping of dielectric liquids: physical model and regime analysis. Phys. Fluids 31(11), 113601–113615 (2019)
3. Yang, L., et al.: Flow distribution control in meso scale via electrohydrodynamic conduction pumping. IEEE Trans. Ind. Appl. 53(2), 1431–1438 (2017)
4. Talaat, M., Essa, M.A.: Effect of electrohydrodynamic stresses in dielectric liquid: simulation study with the aid of single artificial air bubble using level set-volume of fluid method. IET Gener. Transm. Distrib. 13(20), 4694–4701 (2019)
5. Tavari, T., et al.: A systematic overview of electrode configuration in electric-driven micropumps. Electrophoresis 43(13-14), 1476–1520 (2022).
6. Alcayde, V., Vercher-Martínez, A., Fuenmayor, F.J.: Thermal control of a spacecraft: backward-implicit scheme programming and coating materials analysis. Adv. Space Res. 68(4), 1975–1988 (2021)
7. Chen, S., et al.: Capillary driven flow in oval tubes under microgravity. Phys. Fluids 33(3), 032111–032121 (2021)

8. Didion, J.R.: Electrically Driven Single Phase Thermal Management: STP-H5 EHD Experiment. NASA Technical Reports (2016)
9. Castellanos, A.: Electrohydrodynamics. Springer-Verlag Wien, New York (1998)
10. Atten, P.: Electrohydrodynamic instability and motion induced by injected space charge in insulating liquids. IEEE Trans. Dielectr. Electr. Insul. 3(1), 1–17 (1996)
11. Daaboul, M., et al.: Study of the transition from conduction to injection in an electrohydrodynamic flow in blade-plane geometry. J. Electrostat. 88, 71–75 (2017)
12. Yan, Z., et al.: Velocity and turbulence intensity of an EHD impinging dielectric liquid jet in blade–plane geometry. IEEE Trans. Ind. Appl. 49(5), 2314–2322 (2013)
13. Traoré, P., et al.: Numerical investigation of electroconvection induced by strong unipolar injection between two rotating coaxial cylinders. J. Electrostat. 94, 60–66 (2018)
14. Wang, Q., et al.: Chaotic electro-convection flow states of a dielectric liquid between two parallel electrodes. Eur. J. Mech. B Fluid 89, 332–348 (2021)
15. Becerra, M., Frid, H., Vázquez, P.A.: Self-consistent modeling of laminar electrohydrodynamic plumes from ultra-sharp needles in cyclohexane. Phys. Fluids 29(12), 123605–123615 (2017)
16. Chirkov, V.A., Stishkov, Y.K., Sitnikov, A.A.: Simulation of the integral electric current characteristics of unsteady-state current passage through liquid dielectrics. IEEE Trans. Dielectr. Electr. Insul. 22(5), 2763–2769 (2015)
17. Vázquez, P.A., et al.: Dynamics of electrohydrodynamic laminar plumes: scaling analysis and integral model. Phys. Fluids 12(11), 2809–2818 (2000)
18. McCluskey, F.M.J., Perez, A.T.: The electrohydrodynamic plume between a line source of ions and a flat plate-theory and experiment. IEEE Trans. Dielectr. Electr. Insul. 27(2), 334–341 (1992)
19. Malraison, B., Atten, P., Perez, A.T.: Panaches chargés résultant de l'injection d'ions dans un liquide isolant par une lame ou une pointe placée en face d'un plan. J. Phys. III 4(1), 75–85 (1994)
20. Haidara, M., Atten, P.: Role of EHD motion in the electrical conduction of liquids in a blade-plane geometry. IEEE Trans. Ind. Appl. 21(3), 709–714 (1985)
21. Ayegba, P.O., Edomwonyi-Out, L.C.: Turbulence statistics and flow structure in fluid flow using particle image velocimetry technique: a review. Eng. Rep. 2(3), e12138–e12186 (2020)
22. Pan, C., et al.: Review about PD and breakdown induced by conductive particles in an insulating liquid. High Volt. 5(3), 287–297 (2020)
23. Daaboul, M., Louste, C., Romat, H.: PIV measurements on charged plumes-influence of SiO_2 seeding particles on the electrical behavior. IEEE Trans. Dielectr. Electr. Insul. 16(2), 335–342 (2009)
24. Gouriou, C., Traoré, P., Louste, C.: Influence of seeding particle type on velocity measurements in silicone oil under high voltage. IEEE Trans. Ind. Appl. 53(3), 2471–2476 (2017)
25. Traoré, P., et al.: Electrohydrodynamic plumes due to autonomous and nonautonomous charge injection by a sharp blade electrode in a dielectric liquid. IEEE Trans. Ind. Appl. 51(3), 2504–2512 (2015)
26. Wu, J., et al.: Numerical investigation of electrohydrodynamic plumes for locally enhanced cooling in dielectric liquids. IEEE Trans. Ind. Appl. 51(1), 669–678 (2015)
27. Huth, M., Heilos, A.: Fuel flexibility in gas turbine systems: impact on burner design and performance. In: Modern Gas Turbine Systems, pp. 635–684. Woodhead Publishing (2013)
28. John, G., Liu, P.L.F., Pedersen, G.K.: PIV and Water Waves. World Scientific, Singapore (2004)
29. Boomsma, A., et al.: Comparative experimental evaluation of uncertainty estimation methods for two-component PIV. Meas. Sci. Technol. 27(9), 094006–094022 (2016)
30. Nogueira, J., et al.: Quantitative evaluation of PIV peak locking through a multiple Δt strategy: relevance of the rms component. Exp. Fluids 51(3), 785–793 (2011)
31. Yan, Z., et al.: Experimental estimation of the electric force induced by a blade-plane actuator in dielectric liquids. J. Electrostat 71(3), 478–483 (2013)
32. Atten, P., Malraison, B., Zahn, M.: Electrohydrodynamic plumes in point-plane geometry. IEEE Trans. Dielectr. Electr. Insul. 4(6), 710–718 (1998)
33. Vázquez, P.A., Pérez, A., Castellanos, A.: Thermal and electrohydrodynamic plumes. A comparative study. Phys. Fluids 8, 2091–2096 (1996)
34. Kotsovinos, N.: A Study of the Entrainment and Turbulence in a Plane Buoyant Jet. Califonia Institute of Technology, Pasadena (1975)
35. Pham, M.V., Plourde, F., Kim, S.D.: Three-dimensional characterization of a pure thermal plume. ASME J. Heat Transfer 127(6), 624–636 (2005)
36. Deo, R., Mi, J., Nathan, G.: The influence of nozzle aspect ratio on plane jets. Exp. Therm. Fluid Sci. 31(8), 825–838 (2007)
37. Quinn, W.: Upstream nozzle shaping effects on near field flow in round turbulent free jets. Eur. J. Mech. B Fluid 25(3), 279–301 (2006)
38. Papanicolaou, P.N., List, E.J.: Investigations of round vertical turbulent buoyant jets. J. Fluid Mech. 195, 341–391 (1988)
39. Rivière, N.: Étude expérimentale d'une injection turbulente: application au jet impactant une surface libre. Université de Bordeaux I, Bordeaux (2008)
40. Wang, D., et al.: Modelling the low-frequency dielectric response test of insulation oil. IET Electr. Power Appl. 11(3), 323–330 (2017)
41. Atten, P., Elouadie, L.: EHD convection in a dielectric liquid subjected to unipolar injection: coaxial wire/cylinder geometry. J. Electrostat. 34(2-3), 279–297 (1995)
42. Sha, Y., et al.: A study on electric conduction of transformer oil. IEEE Trans. Dielectr. Electr. Insul. 21(3), 1061–1069 (2014)
43. Wu, S., et al.: Effect of surface modification of electrodes on charge injection and dielectric characteristics of propylene carbonate. High Volt. 5(1), 15–23 (2020)
44. Sun, A., Huo, C., Zhuang, J.: Formation mechanism of streamer discharges in liquids: a review. High Volt. 1(2), 74–80 (2016)
45. Yang, L., et al.: Effects of the charge carrier elimination process on oil conductivity decrease under high electric field intensity. IET Sci. Meas. Technol. 14(10), 979–84 (2020)
46. Atten, P.: Mouvement d'un fluide en présence d'un champ électrique. Tech. Ingénieur, GE, 1–12 (1999)

How to cite this article: Yan, Z., et al.: Structural characteristics of electrohydrodynamic jets induced by a blade-plane actuator subjected to highly non-uniform electric fields: parametric investigation through the particle image velocimetry techniques. High Voltage. 8(1), 183–195 (2023). https://doi.org/10.1049/hve2.12293